YALE PEABODY MUSEUM

JOURNAL OF MARINE RESEARCH

The *Journal of Marine Research,* one of the oldest journals in American marine science, published important peer-reviewed original research on a broad array of topics in physical, biological, and chemical oceanography vital to the academic oceanographic community in the long and rich tradition of the Sears Foundation for Marine Research at Yale University.

An archive of all issues from 1937 to 2021 (Volume 1–79) are available through EliScholar, a digital platform for scholarly publishing provided by Yale University Library at https://elischolar.library.yale.edu/.

Requests for permission to clear rights for use of this content should be directed to the authors, their estates, or other representatives. The *Journal of Marine Research* has no contact information beyond the affiliations listed in the published articles. We ask that you provide attribution to the *Journal of Marine Research.*

Primary and secondary intrusions in double-diffusively stable vertical gradients

by Julian A. Simeonov[1]

ABSTRACT

The purpose of this paper is to show that molecularly-driven double-diffusive intrusions can produce significant lateral and vertical double-diffusive mixing even when the initial temperature and salinity are both stably stratified in the vertical. Assuming uniform density-compensated horizontal gradients and periodic disturbances, three-dimensional direct numerical simulations (DNS) for the fastest growing intrusion show that the latter equilibrates due to the generation of salt fingers which reduce the driving buoyancy pressure gradient. The DNS also provided statistical data for a new parameterization of the salt finger fluxes which includes the effects of shear and variable vertical gradients. This parameterization makes it feasible to numerically investigate the subharmonic instabilities of the equilibrium DNS solution. Linearized calculations with parameterized salt fingers show that the vertical and horizontal wavelength of the fastest growing secondary instability are approximately three and fourteen times that of the primary intrusion. Nonlinear simulations show that the equilibrium lateral and vertical double-diffusive fluxes of the secondary mode are an order of magnitude larger than those of the primary intrusion. Numerically determined dependences of the intrusion lateral velocity on the vertical wavelength are compared to previous numerical and experimental work.

1. Introduction

When warm freshwater overlies cold salty water in the ocean, small-scale double-diffusive processes are usually thought to be unimportant. Holyer (1983) showed that horizontal temperature and salinity gradients can destabilize such stratification with respect to lateral intrusions that gain/lose buoyancy as heat is exchanged faster than salt (molecularly) across the interleaving boundaries – essentially a slanted form of salt fingers (Stern, 1960). This interleaving process is also considered unimportant because of the small vertical scale (few meters) of the fastest growing intrusion. One of the motivations for the present work is to show that such molecularly-driven intrusions can give rise to significant lateral mixing when longer vertical wavelengths are produced by a subharmonic instability of shorter waves.

The intrusions discussed here may be relevant to the observations of frontal interleaving between the climatologically important Indonesian Throughflow (4–10 Sv) and Indian

1. Naval Research Laboratory, Marine Geoscience Division, Stennis Space Center, Mississippi, 39529, U.S.A.
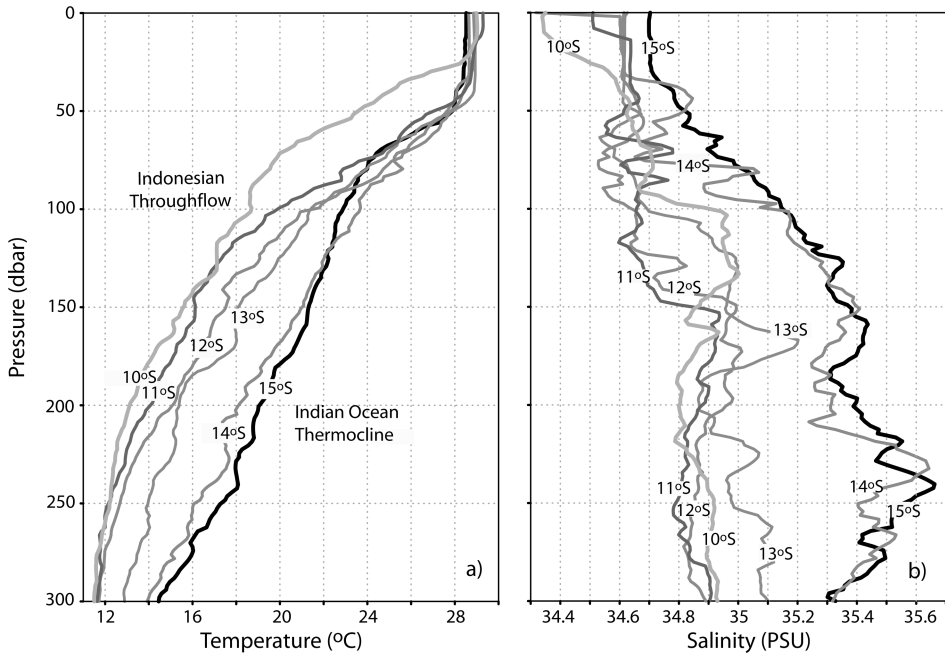*email: simeonov@nrlssc.navy.mil*

Figure 1. Temperature (a) and salinity (b) profiles across the front at 10°S–15°S between the Indonesian Throughflow and Indian Ocean thermocline waters; the interval between profiles is 1 degree of latitude or about 111 km and the vertical resolution is 2 dbar. This CTD data is from the 1995 WOCE section I8N at 80°E (Talley and Baringer, 1997). The 2 dbar data are obtained by filtering and averaging the 25 Hz raw data to 2 Hz, applying a spike removal filter to the 2 Hz data, and applying a ship-roll filter to minimize density inversions during pressure-sequencing of the 2 Hz series.

Ocean thermocline waters. As a result of lateral mixing, the westward flowing Indonesian water loses most of its cold and fresh anomaly by the time it reaches the African coast (Gordon, 2005). Below 100 m the Indonesian waters have nearly uniform salinity (Fig. 1) in the vertical and are stratified mainly by temperature with characteristic density ratios $R \equiv \alpha \bar{T}_z / \beta \bar{S}_z = -10$; closer to the Indian Ocean waters, however, the salinity stratification is as strong as that due to temperature and R approaches -1. In the present study, we will use a spatially uniform density ratio with the intermediate value $R = -5$. For this double-diffusively stable gradient there will be no salt fingers or diffusive convection during the initial stage of linear growth when the intrusion amplitude is small. This is similar to the intrusions on a stable salinity gradient "heated from below" at $R = 0.6$ (Simeonov and Stern, 2008), except that the development of temperature inversions is less likely in the present case of strongly stable background temperature field. As in the $R = 0.6$ case, we expect that salt fingers developing on salinity inversions would play a significant role in the finite amplitude intrusion dynamics.

Motivated by ocean observations, we consider horizontal gradients which are two orders of magnitude smaller than the vertical gradients. This should be contrasted with laboratory interleaving experiments (e.g. Ruddick *et al.*, 1999; Krishnamurti, 2006) where the horizontal gradients are of the same order as the vertical gradients (or even larger initially); the latter is not a realistic representation of an oceanic front. In this connection, the intrusion scales considered in this study – O(1 m) in the vertical and O(1 km) in the horizontal – are 2–3 orders of magnitude larger than the typical laboratory scales. Another major difference between our calculations and laboratory intrusions (also related to the strength of the horizontal gradient) is concerned with the onset of the interleaving process. In the present study, there will be no salt fingers initially and infinitesimal interleaving disturbance amplify solely due to molecular diffusion as in Holyer's (1983) linear theory; small-scale double diffusion would appear only after a relatively long period since a large lateral displacement of the weak horizontal gradient is needed to perturb the initial vertical gradient. In laboratory experiments on the other hand, only a small lateral displacement of the initial strong horizontal gradient is sufficient to destabilize the initial vertical gradient. The appearance of strong double diffusion like salt fingers at the very onset of such experiments results in an intrusion dynamics which is beyond the scope of this paper. Since our focus is on the intrusion scales rather than the scale of the background gradients we consider here the simplest case where the background temperature and salinity vary linearly in the vertical and the horizontal.

Our investigation begins with three-dimensional Direct Numerical Simulations (DNS) of the fastest growing mode of linear theory (Holyer, 1983). The purpose of these DNS is to investigate the equilibration mechanism and to estimate the average horizontal and vertical heat and salt fluxes and their dependence on the horizontal gradients. For the DNS, we use a tilted computational box (Simeonov and Stern, 2008) whose vertical size and slope are given by Holyer's (1983) linear theory. In a preliminary comparison of the 2D and 3D simulations, we found significant qualitative and quantitative difference resulting from the absence of salt fingers in the 2D simulations. Such difference is consistent with our previous work (Stern and Simeonov, 2005b) where we found that strong shear can completely suppress two-dimensional fingers, while the corresponding 3D finger flux remains finite because fingers independent of the downstream direction are not affected by the shear (see also Kimura and Smyth, 2007). Linden (1974) showed that in the presence of shear, the finger variation in the downstream direction is suppressed due to progressive tilting of the vertical finger flow by the shear.

Three-dimensional DNS for wavelengths longer than the fastest growing one would be prohibitively expensive because of increased domain size and much slower growth rates. Furthermore, the intrusion slope remains fixed in the DNS but may actually evolve in a large-scale domain. As long as the dynamics of intrusions considered here involves only salt finger effects, it is possible to model the latter with flux parameterizations and consider only the evolution of large scales. We have previously used a similar approach in studying the amplification of gravity waves by salt fingers (Stern and Simeonov, 2002) using a gradient flux law for salt fingers obtained in the small-domain DNS of Stern *et al.* (2001).

Unfortunately, this gradient flux law is not applicable to intrusions because of the presence of shear and layers in which the vertical gradients remain double-diffusively stable. These effects will be implicitly included in a new gradient flux law obtained from the DNS for the fastest growing intrusion. As shown, a parameterized calculation using the new flux law (Section 3) predicts intrusion amplitudes in excellent agreement with the corresponding three-dimensional DNS.

In the second part of the present work, we use this new flux law for parameterized calculations of intrusions in large computational domains which include wavelengths longer than the fastest growing one (Section 4) and slopes which are free to vary. These calculations will be used to determine the dependence of the maximum intrusion velocity and the lateral heat flux on the vertical wavelength and the horizontal gradient (Section 5). In Section 6, the model results are discussed in relation to intrusion observations associated with Indonesian Throughflow waters and previous laboratory experiments.

2. DNS for the fastest growing primary intrusion

As in the previous DNS, we assume here lateral temperature $\bar{T}_x$ and salinity $\bar{S}_x$ gradients which are density compensated $\alpha \bar{T}_x = \beta \bar{S}_x < 0$, horizontally uniform and unbounded. The molecular heat diffusivity, K_T, and viscosity, ν, are the same as in seawater with a corresponding Prandtl number $\mathrm{Pr} \equiv \nu/K_T = 7$. The salt diffusivity K_S is such that the corresponding diffusivity ratio $\tau \equiv K_S/K_T = 1/96$ is approximately equal to that of seawater. The assumed normal mode intrusions are plane waves with a slope s relative to the horizontal; in a tilted computational domain having the same slope these will be independent of the rotated horizontal axis (ξ).

The governing Navier-Stokes equations are nondimensionalized using the length scale $d \equiv (K_T^2/g\beta|\bar{S}_z|)^{1/4}$, time scale $d^2/K_T = (g\beta|\bar{S}_z|)^{-1/2} \equiv N_S^{-1}$, temperature scale $\beta|\bar{S}_z|d/\alpha$ and salinity scale $|\bar{S}_z|d$; here N_S is the buoyancy frequency for the mean salinity gradient. The velocity scale is K_T/d. Typical ocean values of d and d^2/K_T are respectively 1 cm and 10 min.

Using primes to denote the deviations from the undisturbed basic state, the nondimensionalized equations in the rotated (ξ, y, η) reference frame are:

$$\frac{d\mathbf{v}'}{dt} + \mathrm{Pr}\,\nabla p' = \mathrm{Pr}\,\Delta\mathbf{v}' + (T' - S')\mathbf{G} \tag{1a}$$

$$\nabla \bullet \mathbf{v}' = 0 \tag{1b}$$

$$\frac{dT'}{dt} - \frac{a - Rs}{\sqrt{1+s^2}}u' - \frac{R + as}{\sqrt{1+s^2}}w' = \Delta T' \tag{1c}$$

$$\frac{dS'}{dt} - \frac{a - s}{\sqrt{1+s^2}}u' - \frac{1 + as}{\sqrt{1+s^2}}w' = \tau\Delta S', \tag{1d}$$

$$\frac{d}{dt} \equiv \frac{\partial}{\partial t} + u'\frac{\partial}{\partial\xi} + v'\frac{\partial}{\partial y} + w'\frac{\partial}{\partial\eta}, \quad \nabla \equiv \left(\frac{\partial}{\partial\xi}, \frac{\partial}{\partial y}, \frac{\partial}{\partial\eta}\right)$$

where in (1c,d) the coefficients in front of u' and w' are the undisturbed across-front (ξ) and vertical (η) temperature and salinity gradients,

$$\mathbf{G} = (-s, 1)(1 + s^2)^{-1/2}$$

is a unit vector antiparallel to gravity, and $a \equiv \bar{S}_x / \bar{S}_z$ is the isohaline slope.

Assuming periodic boundary conditions in (ξ, y, η), Eqs. (1) will be solved with the pseudo-spectral Fourier method. The integration in time is performed with a fourth-order Runge-Kutta scheme (RK-4). The along-intrusion L_ξ, and vertical L_η domain sizes are set equal to the fastest growing intrusion wavelength h_*; the spanwise domain size L_y is 0.5 h_*. The calculations presented below are for $R = -5$, Pr $= 7$ and $\tau = 1/96$. For these parameters Holyer's (1983) linear theory gives for the largest growth rate and the corresponding vertical wavelength and slope:

$$\lambda = 0.0517a, \quad h_* = 17.3a^{-1/2}, s = 0.145a. \tag{2}$$

The intrusion equilibration is illustrated here with a calculation for $a = 0.05$ and $h_* = 77.4$ (2). The assumed $L_\xi = L_\eta = 2L_y = 77.4$ domain is resolved on a grid with 256 × 128 × 256 nodes, having a uniform grid step $\Delta x = \Delta y = \Delta z = 0.302$; the time step was $\Delta t = 0.02$. The calculation was initialized with the normal mode intrusion

$$[\bar{u}'(\eta), \overline{T}', \overline{S}'] = [U_0, T_0, S_0] \sin(2\pi\eta / h_*) \tag{3}$$

where for $U_0 = 0.5$, $T_0 = 4.7$ and $S_0 = 8.1$ are determined from the linear theory solution.

The domain averaged horizontal heat flux $\langle \sqrt{(u' + sw')T'} \rangle$ (Fig. 2a, thick gray) shows that the exponential intrusion amplification stops at $t = 500$ when salt fingers (not shown) first develop within the salinity inversions (Fig. 3b) near the top/bottom of the computational domain. After the intrusion growth is interrupted by salt fingers, the horizontal heat flux (Fig. 2a) and the maximum lateral velocity $U_{\max} \equiv \max[\sqrt{u'(\eta)}]$ (Fig. 2b) continue to oscillate around their respective equilibrium values $\langle \sqrt{(u' + sw')T'} \rangle = 13.1 \pm 4.4$ and $U_{\max} = 1.68 \pm 0.3$ (averaged over $600 \le t \le 1500$). The initial fingers are laminar, grow exponentially and produce large vertical fluxes of heat and salt which cause a reduction of the intrusion salinity anomaly (Fig. 3b, profile 15). The fingers then become disorganized with smaller vertical fluxes (Stern and Simeonov, 2005a) which are strong enough to produce well-mixed layers in salinity (Fig. 3b) but not in temperature (Fig. 3a) and density (Fig. 3c). As a result of the weak mixing, no thin interfaces develop as found previously in DNS for stable salinity gradient "heated from below" or finger favorable gradients (Simeonov and Stern, 2007, 2008). The horizontally-averaged vertical density (Fig. 3c) is nearly unchanged from its undisturbed value and the quasi-equilibrium state essentially consists of a thick doubly-stable central region separated by finger-favorable salinity inversions with an overall density ratio $R_f = 20$. The relatively weak fingers corresponding to this density ratio are shown in Figure 4 using two surfaces of constant perturbation salinity $S'(\xi, y, \eta) - \overline{S}'(\eta) =$
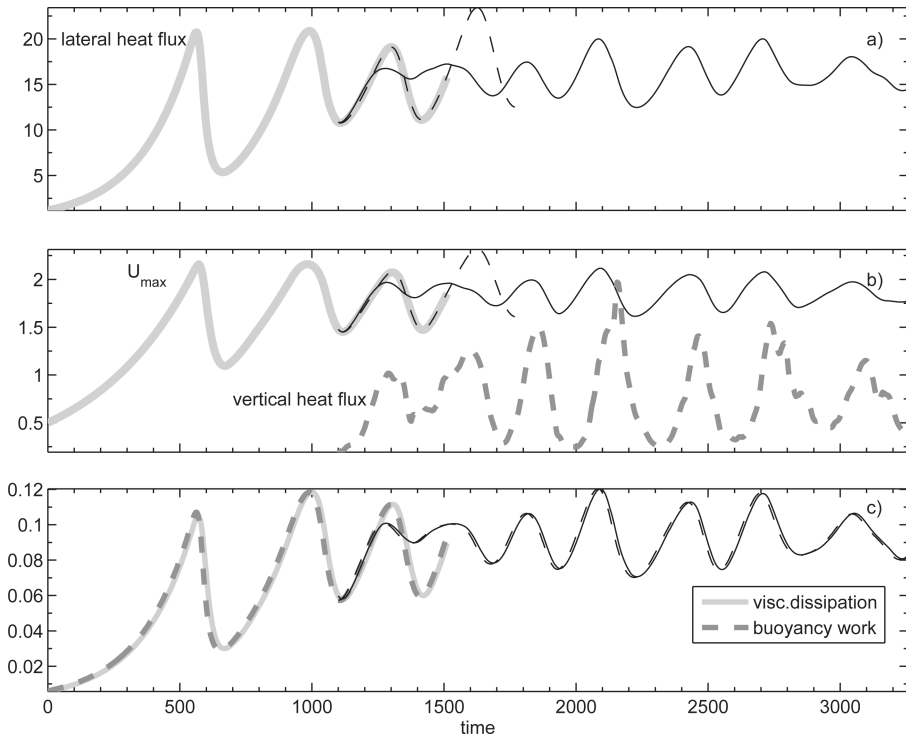
Figure 2. The lateral heat flux (a) and the maximum lateral velocity (b) in the main DNS for $\tau = 1/96$, $a = 0.05$ and $L_\xi = L_\eta = 2L_y = h_*$; this run (thick solid gray) ends at $t = 1600$. The effect of domain size is illustrated in (a) and (b) with two additional simulations for $L_\xi = L_\eta = L_y = h_*$ (dashed) and $4L_\xi = L_\eta = L_y = h_*$ (solid) domains. Also shown in (b) is the vertical heat flux (dark gray dashes) for the $4L_\xi = L_\eta = L_y = h_*$ run. c) The buoyancy work (dashed) and the viscous dissipation (solid) for the main run (thick lines) and the $4 L_\xi = L_\eta = L_y = h_*$ run (thin lines).

± 2. The cross-section of the fingers at the top of the computational box (Fig. 4) shows long streaks stretched along the ξ axis, suggesting that the preferred form of sheared fingers is that of salt sheets, previously observed in the laboratory by Linden (1974).

Figure 4 shows that there are about 4–5 finger pairs in the y-direction. To check the effect of the number of fingers on the intrusion amplitude we next repeat the above calculation in a computational box with twice larger width $L_y = h_*$. The calculation is initialized with the data from the main run at $t = 1100$, extended periodically in the y-direction, and some random noise. The respective lateral heat flux (Fig. 2a dashed) and U_{max} (Fig. 2b dashed) are indistinguishable from those of the $L_y = h_*/2$ run for $1100 \leq t \leq 1500$. Thus, a couple of salt finger pairs in the y-direction appear to be sufficient in modeling this type of finite amplitude intrusions. Because the preferred finger form consists of salt sheets aligned

$$\overline{T'}(\eta) - R\eta$$

$$\overline{S'}(\eta) - \eta$$
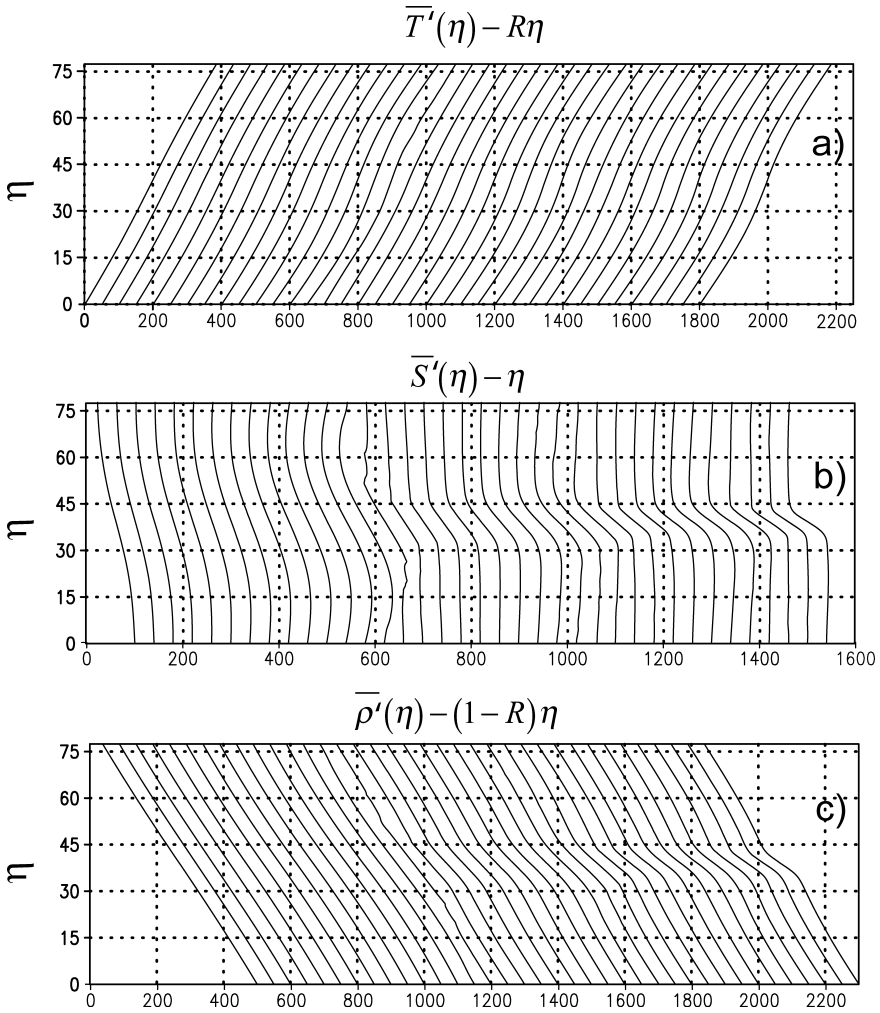

$$\overline{\rho'}(\eta) - (1-R)\eta$$

Figure 3. A time sequence of vertical profiles of the mean temperature (a), salinity (b) and density (c) for the primary calculation in Figure 2. The time interval between profiles is 40 time units and the horizontal offset between profiles is 50. After the salinity inversion (the salt finger layer) forms it persist until the end of the calculation.

with the flow, it is plausible that some reduction of the ξ-domain size will not affect the equilibrium intrusion amplitude. This is shown by the run with $L_\xi = h_*/4$ (Fig. 2a,b solid line) where the equilibrium $U_{max} = 1.86 \pm 0.13$ and $\langle \sqrt{(u' + s w')T'} \rangle = 16.1 \pm 1.9$ imply an amplitude that is only about 10% larger.

The terms in the equation for the rate of change of the mean kinetic energy $\overline{u'^2}/2$ (Fig. 2c) suggest that an approximate balance between buoyancy production $s\langle (\overline{T'} - \overline{S'})\overline{u'} \rangle$ (dashed)
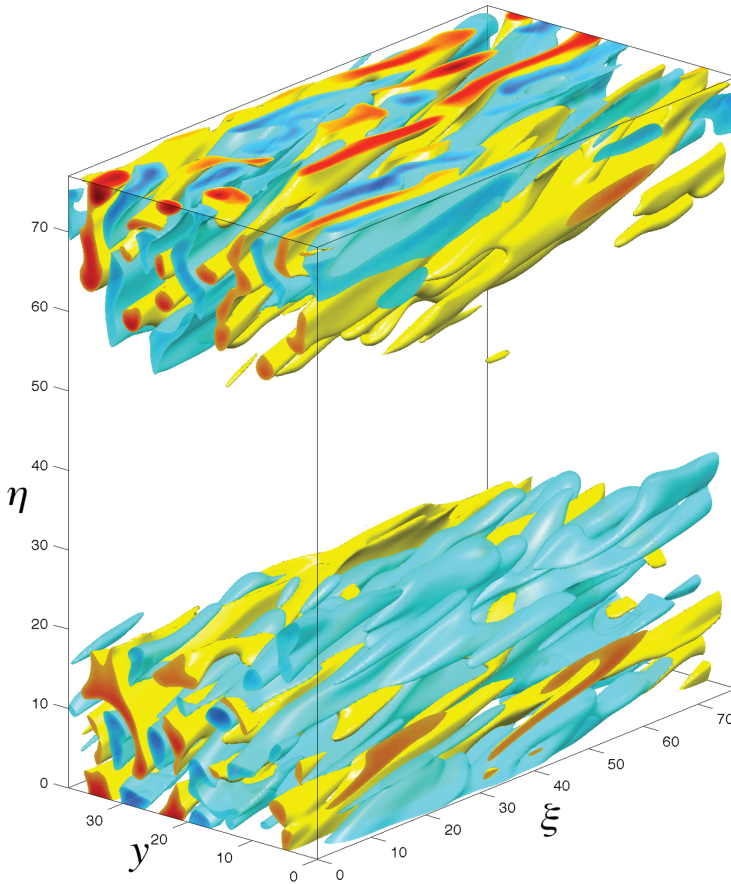
Figure 4. A volumetric plot of two surfaces of constant perturbation salinity $S'(\xi, y, \eta) - \overline{S}'(\eta) = \pm 2$ at $t = 1512$; the positive/negative isohaline surface is shown in yellow/blue. To emphasize the small-scale, the large amplitude signal of the mean intrusion $\overline{S}'(\eta)$ is removed. A color scheme, using red/dark blue for high/low salinity shows "interior" salinity variation where the two isohaline surfaces intersect the domain sides.

and viscous dissipation $\mathrm{Pr}\langle(\partial \overline{u}'/\partial \eta)^2\rangle$ (solid) exists from the beginning of the calculation. Compared to these terms, the Reynolds stress work (not shown) is three orders of magnitude smaller and the small difference between buoyancy production and viscous dissipation in Figure 2c is essentially the small rate of change of $\overline{u}'^2/2$. The buoyancy-viscous balance implies that the magnitude of U_{max} is controlled by the intrusion buoyancy anomaly. This should be contrasted with Simeonov and Stern (2007) where the intrusion momentum was strongly damped by Reynolds stresses after the onset of double-diffusively driven mixed layer convection.
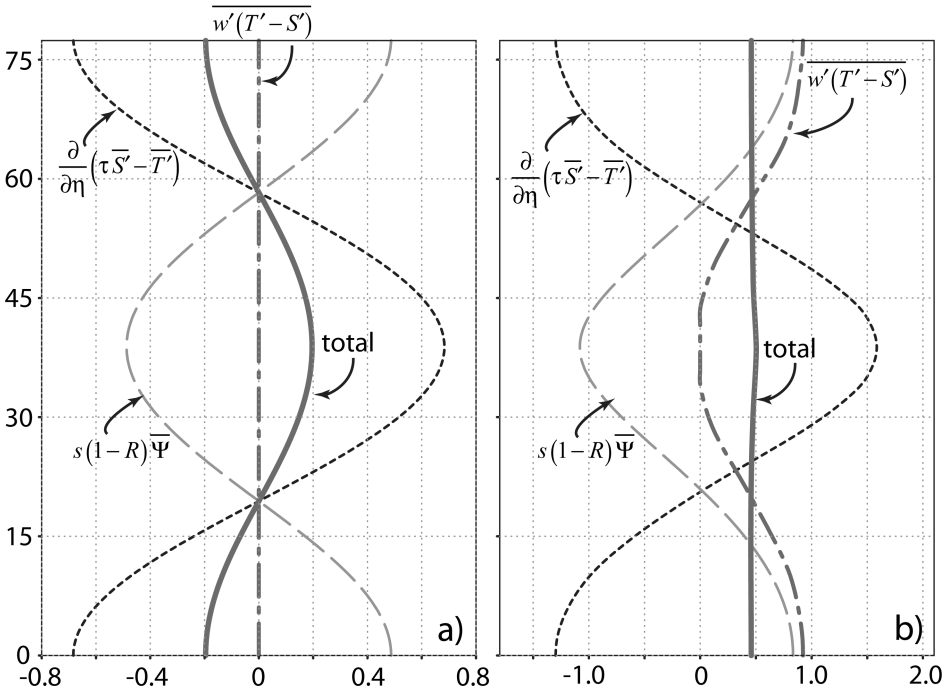
Figure 5. The vertical buoyancy fluxes (4) due to molecular diffusion (short dashes), advection of the basic state (long dashes), salt finger convection (dash-dot) and their sum (thick line) at $t = 240$ (a) and time-averaged ($1500 \leq t \leq 3200$, Fig. 2) in the final quasi-steady state (b).

Next, we show that the intrusion $T - S$ amplitude equilibrates because the salt fingers tend to oppose the buoyancy anomalies produced by molecular diffusion. The effect of the salt fingers can be illustrated using the equation for the rate of change of the horizontally averaged density perturbation:

$$\frac{\partial \overline{\rho}'}{\partial t} = \frac{\partial}{\partial \eta} \left[\frac{\partial (\tau \overline{S}' - \overline{T}')}{\partial \eta} + \overline{w'(T' - S')} + s(1 - R)\overline{\Psi}' \right], \tag{4}$$

where $\frac{\partial \overline{\Psi}'}{\partial \eta} \equiv -\overline{u}'$. In Eq. (4), the first term is the molecular diffusion, the second is the salt finger flux and the third one is the displacement of the undisturbed density gradient by the intrusion. These terms are shown in Figure 5 for an early time corresponding to linear growth (left panel) and for the final equilibrium (right panel). During the linear growth $t = 240$ the buoyancy fluxes are dominated by molecular diffusion (Fig. 5a, short dashes) and this produces the buoyancy anomalies that drive the intrusion; at this time there are no salt fingers and $\overline{w'(T' - S')} = 0$. In the final state, the salt fingers and the $s(1 - R)\overline{\Psi}'$ term

Table 1. The maximum nondimensional lateral velocity $U_{\max}$ and the corresponding horizontal heat flux $\langle \overline{(u' + sw')T'} \rangle$ in three-dimensional DNS for $R = -5$, $\tau = 1/96$ and different $a \equiv \bar{S}_x/\bar{S}_z$ with their corresponding vertical domain size L_η and grid size; approximately the same grid step (about 10% variation) is used in all runs. Two of the $a = 0.02$ runs use slope smaller than the fastest growing one.

$a \equiv \bar{S}_x/\bar{S}_z$	s	L_η	$U_{\max}$	$\langle \overline{(u' + sw')T'} \rangle$	Ri_0	Grid size
0.05	$0.145a$	77.4	1.86	16.1	740	$64 \times 128 \times 256$
0.02	$0.145a$	122.3	3.0	38.5	693	$128 \times 128 \times 384$
0.02	$0.120a$	122.3	2.9	32.4	638	$128 \times 128 \times 384$
0.02	$0.090a$	122.3	2.6	22.8	693	$128 \times 128 \times 384$
0.01	$0.145a$	173	4.1	87	831	$128 \times 128 \times 512$

result in a complete cancellation of the molecular buoyancy flux divergence so that the total flux divergence is approximately zero (Fig. 5b, solid).

Some comments are due concerning the heat flux and velocity oscillations in Figure 2a,b. These oscillations do not seem to result from the interaction of salt fingers with the internal gravity wave having the same slope as the computational domain (cf. Stern and Simeonov, 2002) as the period of the oscillations changes in time. Furthermore, the buoyancy and velocity oscillations are clearly in-phase (Fig. 2a,b). Figure 2b also shows that there is a time lag of about 100 time units between the maximum finger fluxes (dark grey dashes) and the intrusion amplitude (thin solid). We suggests that this time lag is the result of the finite time it takes the salt finger flux to adjust to changes in the intrusion amplitude (and vertical gradients). Such an effect will be absent in the parameterized simulations where the finger flux adjusts instantaneously to changes in the vertical gradients; it will be shown that the absence of the oscillations in the parameterized simulations does not affect the time-averaged intrusion amplitude (Section 3b).

For the purpose of developing a parameterization of salt fingers in the intrusions considered here, several additional DNS (Table 1) for smaller values $a = 0.02$, 0.01, as well as slopes smaller than the fastest growing one, were also made. (It is expected that larger-scale secondary instabilities will have a bias towards smaller slopes.) Having shown (Fig. 2) that the intrusion equilibration can be modeled with L_ξ and L_y smaller than h_*, the $a = 0.02$ and $a = 0.01$ runs use respectively $3L_\xi = L_\eta = 3L_y = h_*$ and $4L_\xi = L_\eta = 4L_y = h_*$ computational domains; the corresponding grid sizes given in the Table 1 greatly reduce the computational requirements. The DNS results for the fastest growing slope $s = 0.145a$ (Fig. 6, $\bigcirc$) also suggest the following linear dependence relating $U_{\max}$ to the intrusion thickness L_η:

$$U_{\max} = 0.024L_\eta. \tag{5}$$

This dependence of $U_{\max}$ on L_η will be compared below with the results of the nonlinear parameterized calculations obtained in Section 5.
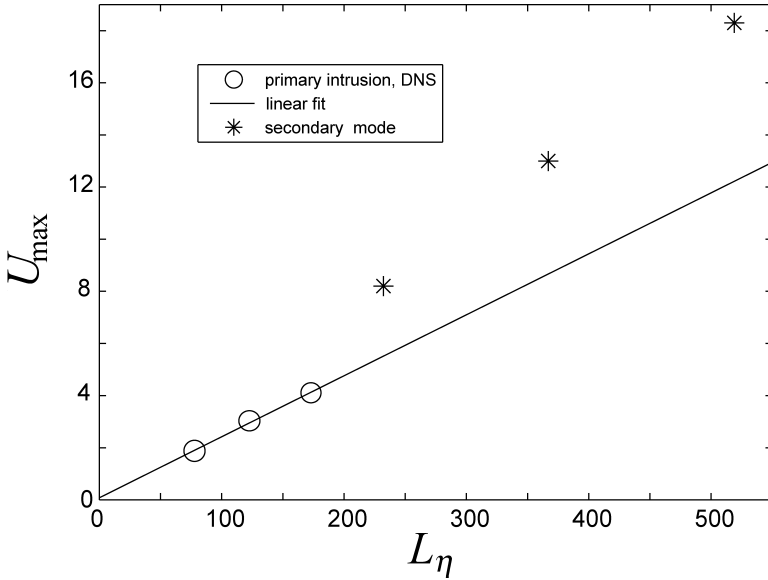
Figure 6. The maximum lateral velocity (○) for the DNS in Table 1 as a function of the layer
thickness. The straight line is a linear fit passing through the origin and having a slope of 0.024.
Also shown is the maximum lateral velocity (Σ) of the fastest growing secondary instability modes
for $a = 0.05$, 0.02 and 0.01 obtained with parameterized calculations in Section 5.

3. A model for the fastest growing primary intrusion with parameterized salt finger fluxes

a. Gradient flux law for salt fingers in intrusions for $R = -5$

Here, the DNS from the previous section are used to obtain a parameterization for salt
fingers which are influenced by the intrusion shear and are limited to a region of finite
depth. The nondimensionalization in Section 2 implies the following parametrization for
the nondimensional vertical heat F_H and salt F_S fluxes:

$$F_H = -Nu(\bar{T}'_\eta - R), \tag{6a}$$

$$F_S = F_H/\gamma, \tag{6b}$$

where the Nusselt number Nu and the salt finger flux ratio γ will be obtained from the DNS
in Table 1. The Nusselt number and the flux ratio are computed as horizontal/time averages
from the final quasi-steady state:

$$Nu = -\frac{\overline{(w' - su')T'} + s\overline{u}'\overline{T}'}{\bar{T}'_\eta - R}. \tag{6c}$$

$$\gamma = \frac{\overline{(w' - su')T'} + s\overline{u}'\overline{T}'}{\overline{(w' - su')S'} + s\overline{u}'\overline{S}'}. \tag{6d}$$
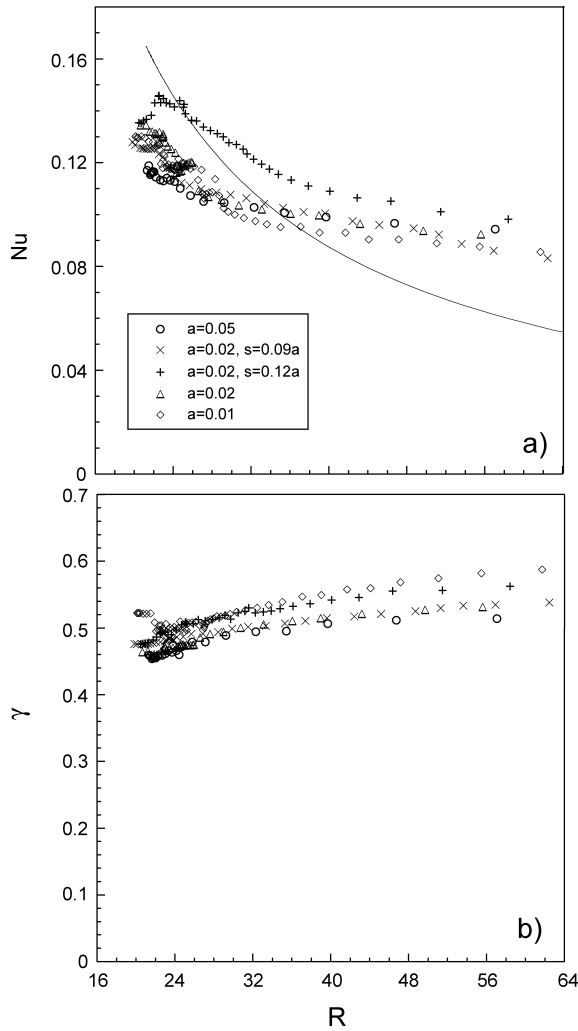
Figure 7. The local Nusselt number Nu (a) and flux ratio γ (b) as a function of the local density ratio in the intrusion DNS (Table 1). The solid line in (a) is $Nu = 3.5R^{-1}$. The plot excludes the central region where the finger flux is zero (Fig. 5b, dash-dot) and the density ratio is negative. The R^{-1} fit in (a) gives more weight to the slope of $Nu(R)$ at low R.

Note that in (6c,d) the vertical intrusion heat flux $-s\overline{u'}\,\overline{T}'$ is removed from the total vertical flux $\overline{(w' - su')T'}$; the same procedure was used for the vertical salt flux in (6d). The Nusselt number and the flux ratio are plotted on Figures 7a,b as a function of the horizontally/time averaged local density ratio:

$$R'(\eta) = \frac{\bar{T}'_\eta - R}{\bar{S}'_\eta - 1}. \tag{7a}$$

The Richardson number Ri_0 based on the maximum shear in the finger layer (at $\eta = 0$) and the basic state density gradient

$$Ri_0 = \frac{(1 - R)}{\left[\overline{u'_\eta}(\eta = 0)\right]^2} \tag{7b}$$

given in Table 1 shows that the shear acting on the salt fingers is quite weak.

Nevertheless, the weak fingers at $R' = 20$ are strongly affected by this shear as their $Nu = 0.14$ is an order of magnitude smaller than the corresponding $Nu = 1.06 \exp(5.62/R')$ for fingers in the absence of shear (Stern *et al.*, 2001). The reduction of the finger flux with shear is consistent with previous laboratory and numerical experiments (Fernandes and Krishnamurti, 2010; Kimura *et al.*, 2011; Stern and Simeonov, 2005b).

Motivated by the numerical reasons discussed below, we propose the following functions to fit the numerical data on Figure 7:

$$Nu = 3.5/R', \gamma = 0.45; \tag{8}$$

although these are not explicit functions of the Richardson number the effect of shear is implicit in the numerical constants in (8). We note that the above R^{-1} fit is not chosen to minimize least square errors but the errors in the slope of $Nu(R)$ at low R. This slope is what produces the vertical divergence of the salt finger flux that is responsible for the intrusion equilibration and, therefore, is the main feature of interest here. From (6a), (7a) and (8) we obtain the following very simple formula for the heat flux:

$$F_H = \begin{cases} -3.5\left(\overline{S'_\eta} - 1\right) & where \quad \overline{S'_\eta} \geq 1 \\ 0 & where \quad \overline{S'_\eta} < 1 \end{cases} \tag{9}$$

which is valid for all x and z. The discontinuity at $\overline{S'_\eta} = 1$ will be smoothed with a 2nd order finite-difference de-aliasing filter (Lele, 1992), which suppresses variations at the grid scale $2\Delta z$. We note that instead of the piece-wise continuous formula (9) it is also possible to use exponential function fits $Nu(R)$ which smoothly extend F_H for all values of x and z (including the salinity interface region characterized with negative R). Although this may be attractive for analytical calculations, it is not suitable for spectral simulations where the intrinsic nonlinearity of the exponential function magnifies short wave variations in the flux that lead to numerical instabilities. Less severe, but similar numerical problems are also caused by power fits $Nu(R)$ with large exponents.

b. Comparison with DNS

To test the proposed flux formulas (9, 6b), here we compare the results of a parameterized calculation for $a = 0.05$ with the corresponding DNS (Section 2). The governing equations are the two-dimensional (x, z) Eqs. (1) in a nonrotated reference frame $(s = 0)$, further modified by adding the vertical divergence of the salt finger fluxes $\partial F_H/\partial z$ and $\partial F_S/\partial z$, respectively, to the l.h.s. of Eqs. (1c, d):
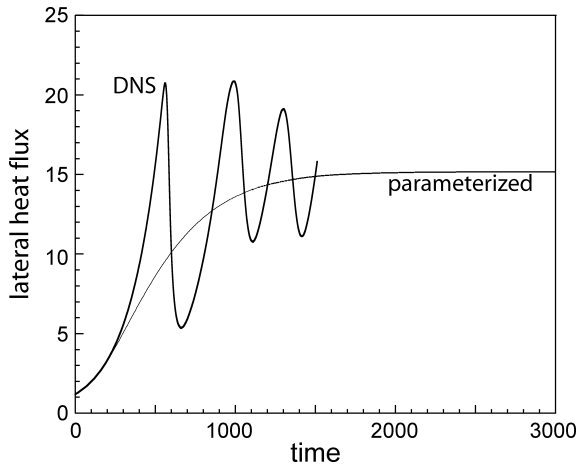
Figure 8. The lateral heat flux as a function of time in the parameterized run for $R = -5$, $a = 0.05$ (light) compared with the corresponding DNS heat flux (dark, also Fig. 2).

$$\frac{d\mathbf{v}'}{dt} + \text{Pr}\,\nabla p' = \text{Pr}\,\Delta\mathbf{v}' + (T' - S')\mathbf{G} \qquad (10a)$$

$$\nabla \bullet \mathbf{v}' = 0$$

$$\frac{dT'}{dt} - au' - Rw' = \Delta T' - \frac{\partial F_H}{\partial z} \qquad (10b)$$

$$\frac{dS'}{dt} - au' - w' = \tau\Delta S' - \frac{\partial F_S}{\partial z}. \qquad (10c)$$

The effect of the very small salt finger Reynolds stress (Section 2a) is omitted in (10a). In (10a) there is no turbulent eddy viscosity (cf Mueller *et al.*, 2007) which is acceptable as long as the intrusion shear/density profiles remain stable with respect to shear/gravitational instabilities.

The same Fourier spectral method is used to solve the equations numerically. The salt finger terms are obtained from (9,6b) by first computing the fluxes in the physical space and then evaluating the vertical derivatives spectrally. The domain length and height are $h_*/s = 10676$ and $h_* = 77.4$, respectively, essentially resolving one horizontal and vertical wavelength of the fastest growing intrusion. The computational grid had 64 grid nodes in both x and z, resulting in grid steps of $\Delta x = 166.7$ and $\Delta z = 1.21$. In the presented calculation a time step $\Delta t = 0.1$ is used. The calculation was initialized with the normal mode (3) with amplitude $U_0 = 0.5$.

The lateral heat flux in Figure 8 (light) shows that at this relatively large amplitude the intrusion grows much slower than both the DNS and linear theory prediction. In preliminary test with smaller initial amplitude, however, the intrusion grew at a rate very close to the linear theory one. Another difference from the DNS is the absence of the nonlinear
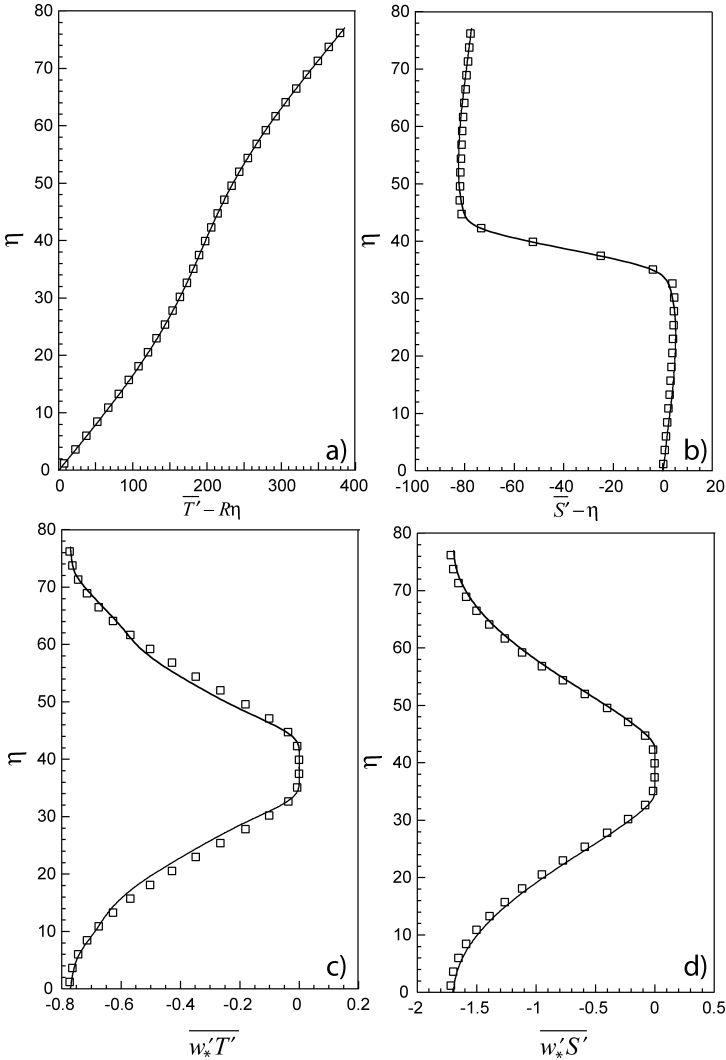
Figure 9. Comparison of profiles of total temperature (a), salinity (b), salt finger heat flux (c) and salt flux (d) in the final quasi-steady state of the 3D DNS (solid line) and the corresponding parameterized calculation ("□") for $R = -5$, $a = 0.05$. The DNS profiles are horizontal/time averages. The profiles of the parameterized run are from the end of the calculation at $x = 0$.

oscillations. Nevertheless, Figure 8 shows that over a comparable time interval the intrusion in the parameterized calculations reaches a steady state with a heat flux $\langle \overline{u'T'} \rangle = 15.2$ which differ by no more than 10% from that in the DNS (Table 1); the corresponding maximum lateral velocity $U_{\max} = 1.81$ is also comparable to the DNS. The predicted profiles (Fig. 9,

"□") of mean temperature and salinity and small-scale fluxes of heat and salt agree closely with those in the DNS (Fig. 9 solid line). As a final test, two additional runs were made for the fastest growing intrusions corresponding to $a = 0.02$ and 0.01; we use the same number of grid points as before but the time steps were $\Delta t = 0.2$ and $\Delta t = 0.5$ for $a = 0.02$ and 0.01, respectively. The respective equilibrium heat flux and lateral velocity were $\langle \overline{u'T'} \rangle = 37.9$ and $U_{max} = 2.87$ for $a = 0.02$, and $\langle \overline{u'T'} \rangle = 75.9$ and $U_{max} = 4.05$ for $a = 0.01$. These also agree closely with the DNS results in Table 1. The overall good agreement suggests that the chosen parameterization (Section 3a) may be useful in obtaining realistic estimates of the amplitude of intrusion scales larger than the fastest growing one (Section 5). Before turning to the question of finite amplitude, we first investigate the stability of the steady state solution obtained in this section.

4. The secondary instability of the equilibrium steady-state primary intrusion.

Previous DNS (Simeonov and Stern, 2008) suggest that the quasi-equilibrium solutions for the primary intrusion are subject to subharmonic instabilities which give rise to longer vertical wavelengths. Due to the inherent limitation of the tilted box DNS, in Simeonov and Stern (2008) the slope of the secondary modes was forced to be the same as that of the fastest growing intrusion. The slope of the fastest growing secondary instability, however, may differ from that of the primary intrusion. Since it is not computationally feasible to include explicitly the horizontal intrusion scales in a DNS we will investigate the subharmonic instabilities with the parameterized model developed in Section 3. The goal of this section is to get some guidance in selecting appropriate domain sizes for the nonlinear calculations in Section 5; the assumption is that in a larger domain the solution will be dominated by the fastest growing secondary instability. Therefore, here we are not interested in a detailed linear theory study of the secondary instability but only in a rough estimate of the horizontal and vertical wavelength of the fastest growing secondary mode.

Because of the model implementation which involves numerical smoothing of the flux F_H, a piece-wise linear function of $\bar{S}'_z$, it is not possible to explicitly linearize this term in (10). Furthermore, the basic steady-state (Fig. 9) is not a monochromatic plane wave and the normal mode of its subharmonic instability would be composed of a large number of Fourier modes. Due to the advective product terms in (10) a linearized calculation would be as computationally expensive as a fully nonlinear one. We will, therefore, not use the traditional method where Eqs. (10) are linearized about the basic state, but the power iteration method which allows us to compute the fastest growing mode directly from the nonlinear equations. In this method, a small random noise perturbation of given initial amplitude is added to the steady-state solution and the nonlinear equations are integrated for a short period of time so that the perturbation amplitude remains small (preferably less than a few % relative amplitude) compared to that of the steady-state solution. The perturbation is then renormalized back to its initial amplitude and the equations are integrated again. After many iterations of this step only the fastest growing perturbation survives the recurrent

Table 2. The growth rate of the dominant secondary instability mode for $a = 0.05$ in computational domains with given L_z and L_x. Note, that a mode with horizontal and vertical wavelength L_x and L_z is not the dominant one when its harmonics grow faster. The table indicates that mode 14×3 is the fastest growing mode.

L_z	L_x	Growth rate
$2\,h_*$	$2\,h_*/s$	$\sigma_{2\times2} = 1.42 \times 10^{-3}$
	$3\,h_*/s$	$\sigma_{3\times2} = 1.48 \times 10^{-3}$
	$4\,h_*/s$	$\sigma_{4\times2} = 1.54 \times 10^{-3}$
	$5\,h_*/s$	$\sigma_{5\times2} = 1.55 \times 10^{-3}$
	$6\,h_*/s$	$\sigma_{6\times2} = 1.54 \times 10^{-3}$
	$8\,h_*/s$	$\sigma_{8\times2} = 1.48 \times 10^{-3}$
$3\,h_*$	$2\,h_*/s$	$\sigma_{2\times3} = 1.05 \times 10^{-3}$
	$4\,h_*/s$	$\sigma_{4\times3} = 1.22 \times 10^{-3}$
	$8\,h_*/s$	$\sigma_{8\times3} = 1.55 \times 10^{-3}$
	$12\,h_*/s$	$\sigma_{12\times3} = 1.64 \times 10^{-3}$
	$14\,h_*/s$	$\sigma_{14\times3} = 1.65 \times 10^{-3}$
	$16\,h_*/s$	$\sigma_{16\times3} = 1.63 \times 10^{-3}$
	$20\,h_*/s$	$\sigma_{10\times3} = 1.61 \times 10^{-3}$
$4\,h_*$	$4\,h_*/s$	$\sigma_{4\times2} = 1.54 \times 10^{-3}$
	$12\,h_*/s$	$\sigma_{6\times2}(\sigma_{4\times2}) = 1.54 \times 10^{-3}$
	$16\,h_*/s$	$\sigma_{5\frac{1}{3}\times2} = 1.55 \times 10^{-3}$
	$20\,h_*/s$	$\sigma_{5\times2} = 1.55 \times 10^{-3}$
	$24\,h_*/s$	$\sigma_{4\frac{4}{5}\times2} = 1.54 \times 10^{-3}$

amplitude reduction. Note that in a normal mode the amplitudes of temperature, salinity and velocity are not independent; thus, the perturbation T, S and $\mathbf{v}$ must be reduced by the same factor during renormalization. In our implementation we renormalize using the temperature amplitude.

In the following we consider only periodic modes having x- and z-wavelengths of mh_*/s and nh_* with integer m and n; such modes will be denoted as $m \times n$. When mode $m \times n$ grows faster than all other modes with shorter wavelengths its spatial structure and growth rate can be obtained with the power iteration method in a computational domain having $L_x = mh_*/s$ and $L_z = nh_*$; this will usually be the case if we consider the band of wavelengths shorter than that of maximum growth. Thus, the maximum growth rate will be determined by applying the power iteration to successively larger domains, beginning with the smallest one having $L_x = 2h_*/s$ and $L_z = 2h_*$. It should be mentioned that modes with noninteger m and n are also valid solutions but will not be considered (explicitly) since they require much larger computational domains; for example, the mode with $m = 5\frac{1}{3}$ will appear as the third harmonics in a computational domain with $L_x = 16h_*/s$.

The results of our power iteration calculations for the secondary instability of the $a = 0.05$ primary intrusion are shown in Table 2. Mode 5×2 grows the fastest among all modes

with $n = 2$ (Table 2, fourth row) and has a growth rate $\sigma_{5\times2} = 0.155 \times 10^{-2}$, which is only two times smaller than the growth rate λ of the corresponding primary intrusion (2). The temperature and velocity distribution of mode 5×2 (Fig. 10a,c) consist of a sequence of elongated closed cells with local slope equal to that of the primary intrusion. The corresponding salinity field (Fig. 10b) has large-gradient interfaces which also line up with the salinity interfaces of the primary mode (Fig. 10, gray lines). The closed cells form a frontal line with slope equal to sn/m. The number of cells depends on the ratio of m and n and is zero (plane wave) when $m = n$. These cellular modes are similar to the secondary instability modes considered by Kerr (1992) and Walsh and Carmack (2003), and can generally be expected when the horizontal gradients vary (Niino, 1986); in our case the horizontal gradients are modified by the finite amplitude primary intrusion.

Note, that mode 8×2 in Table 2 has a growth rate smaller than that of mode 4×2 which is also resolved in the computational domain with $L_x = 8h_*/s$ and $L_z = 2h_*$. To determine the growth rate of mode 8×2 with power iteration it was necessary to periodically remove the two projections of the perturbation on mode 4×2; in this domain there are two independent modes 4×2 with a horizontal phase difference of $1h_*/s$. The number of projections increases rapidly with the domain size and this procedure will not be used for the rest of the calculations in Table 2 where the mode with wavelengths L_x and L_z grows slower than its harmonics; in such cases, we give in the table the growth rate of the harmonics. Since we are interested only in the maximum growth rate we can stop our search when upon further increase of the domain size we have only dominant harmonic modes. Table 2 shows that the latter occurs for $L_z > 3h_*$ and implies that the fastest growing secondary instability is approximately represented by mode 14×3.

We have made similar power iteration calculations for $a = 0.02$ and $a = 0.01$ (not shown) where we again find that mode 14×3 is the fastest growing secondary instability mode. Figure 11 shows that the growth rate of this mode is a linear function of a:

$$\sigma_{14\times3} = 0.033a \tag{11a}$$

like the growth rate of the primary instability (2). Likewise, the vertical wavelength $h_{14\times3}$ and the slope $s_{14\times3}$ of the fastest growing secondary mode have the same dependence on a as the primary instability (2):

$$h_{14\times3} = 51.9a^{-1/2}; \quad s_{14\times3} = 0.031a, \tag{11b}$$

but the slope is 4–5 times smaller than that of the primary intrusion. These results will be used for the nonlinear calculations in the following section.

5. Nonlinear calculations for the fastest growing secondary mode

Here, we will estimate the equilibrium heat flux and maximum lateral velocity of the fastest growing secondary instability mode with parameterized calculations for three different values of $a = 0.05$, 0.02 and 0.01. Accordingly, we use a computational box with
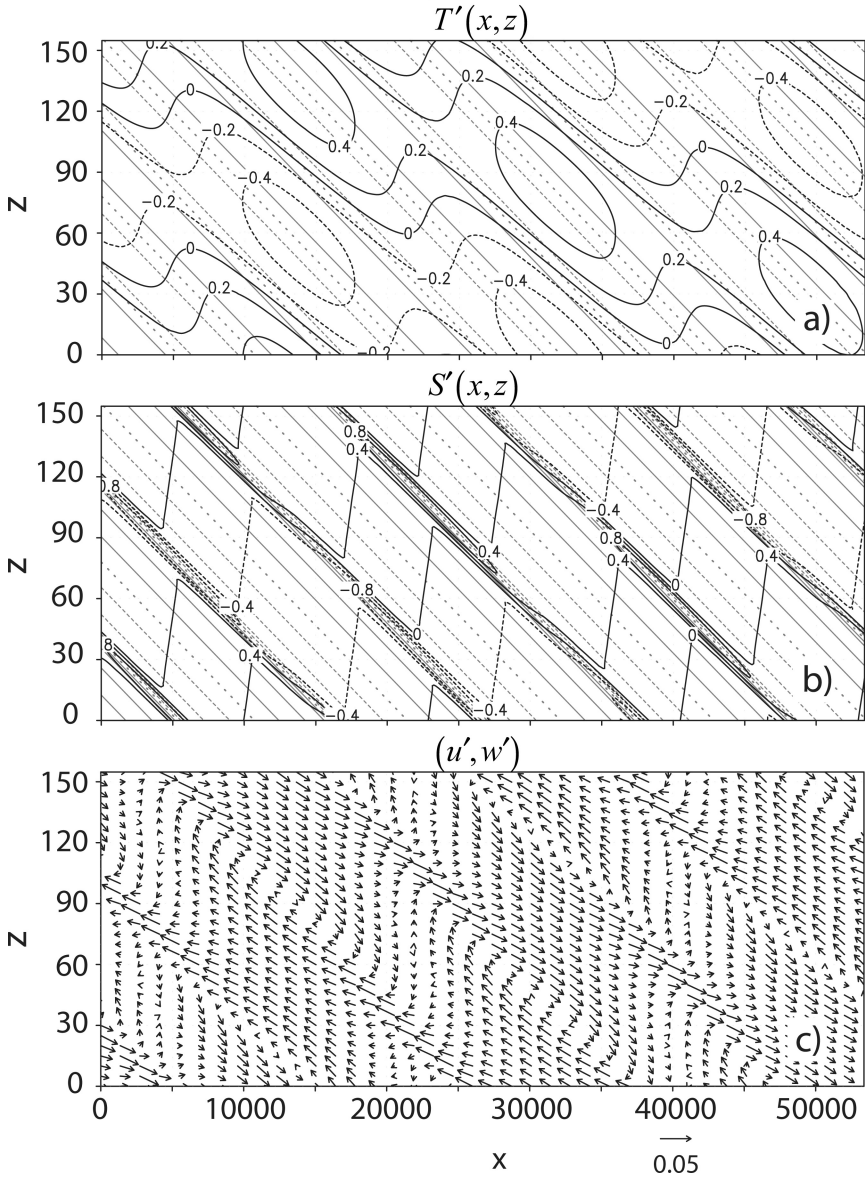
$T'(x,z)$

$S'(x,z)$

(u',w')

Figure 10. Temperature (a), salinity (b) and velocity (c) of the secondary instability mode for $a = 0.05$ obtained with the power iteration in a domain having $L_x = 5h_*/s$ and $L_z = 2h_*$. Also shown in (a) and (b) are the temperature and salinity of the primary intrusion; positive values are solid gray lines, negative values are dashed gray and the zero is gray dots. The horizontal scale is decreased by a factor of 131.
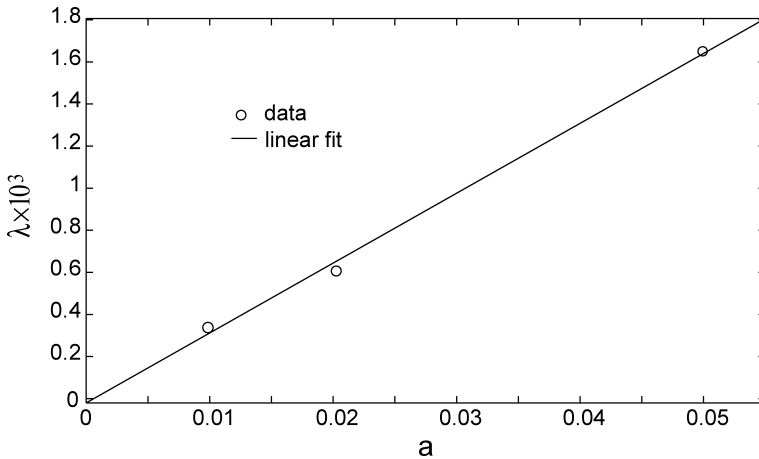
Figure 11. The growth rate ($\bigcirc$) of the fastest growing secondary mode 14×3 for three different $a = 0.05, 0.02$ and 0.01. The solid line is the linear fit in Eq. (11a).

$L_x = h_{14 \times 3}/s_{14 \times 3}$ and $L_z = h_{14 \times 3}$, and the same grid steps and time steps as in Section 3b. The initial condition for T, S, u and w consisted of the steady-state equilibrium primary mode of Section 3b and the corresponding fastest growing secondary instability mode of Section 4; the latter had an rms temperature amplitude equal to 0.3.

The finite amplitude evolution of the secondary instability for $a = 0.05$ is illustrated by three snapshots of the temperature field (Fig. 12), and by the averaged horizontal heat flux (Fig. 13a) and the terms in the equation for the rate of change of the total kinetic energy (Fig. 13b). Figure 13b shows that the intrusion remains in a close balance between buoyancy work and viscous energy dissipation during the entire simulation. This suggests that the secondary mode amplification and subsequent equilibration is controlled by the evolution of the buoyancy perturbation (discussed below). For the initial period $0 < t < 2500$ (Fig. 13a) the perturbation amplifies exponentially with the same growth rate (to three significant digits) as that predicted by (11a). At $t = 2000$ (Fig. 12b) the secondary mode is already apparent in the numerical solution and has an amplitude which is about two times larger than that of the solution at $t = 0$ (Fig. 12a). After $t = 3000$ (Fig. 13) the solution grows approximately linearly at much slower rate and the closed cells begin to merge so that at time $t = 5000$ (Fig. 12c) the solution is already a simple plane wave with slope equal to $s_{14 \times 3}$; this simple plane wave solution persists until the end of the simulation. At $t = 7000$ the heat flux begins to equilibrate at $\langle \overline{u'T'} \rangle = 567.7$ (Fig. 13a) which is an order of magnitude larger than that of the primary mode. A mild density inversion develops for $t > 7000$ just below and above the main density interface (Fig. 14a) and gives rise to very weak overturning instabilities which manifest as short x-wavelength noise. The noise has a negligible effect on the time-averaged large-scale solution (Fig. 14a,b black) which is essentially the same
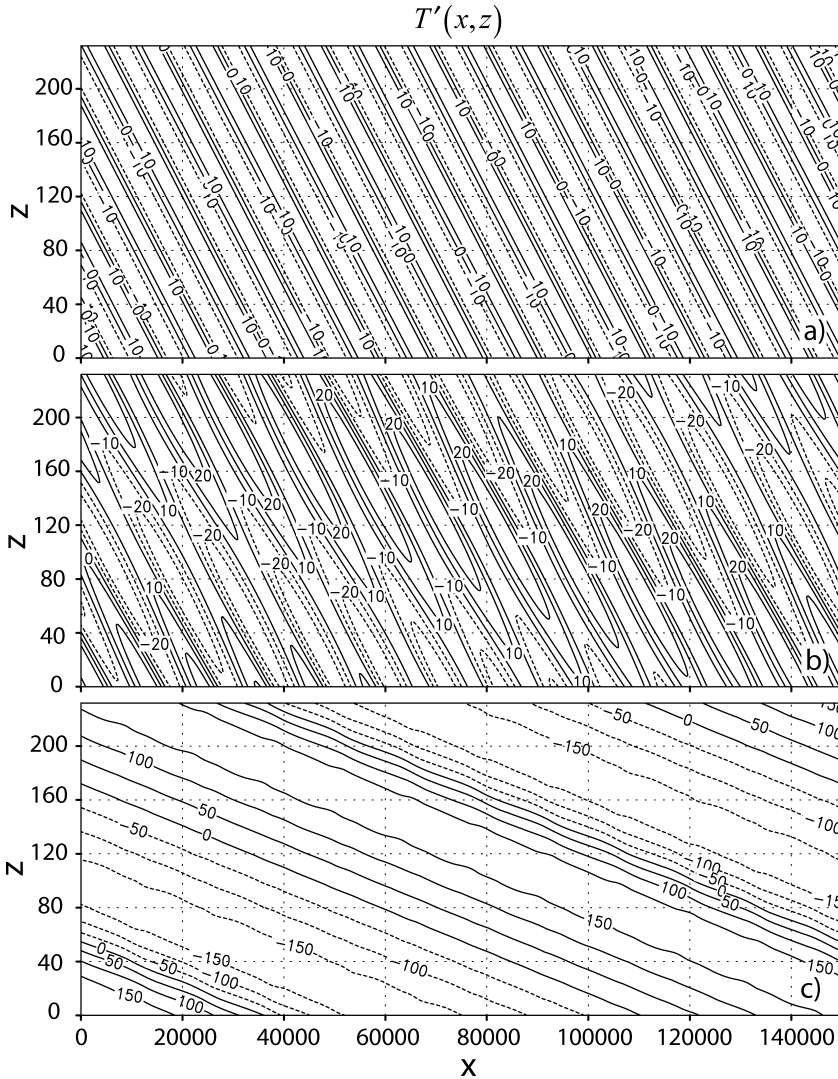
$$T'(x,z)$$

Figure 12. The perturbation temperature at three different times $t = 0$ (a), $t = 2000$ (b) and $t = 5000$ (c) showing the finite-amplitude evolution of the secondary instability mode in a nonlinear simulation for $a = 0.05$.

as the instantaneous solution at $t = 7000$ (Fig. 14a,b gray) when the noise is absent. The maximum lateral velocity of the final steady-state solution $U_{max} = 8.2$ (Fig. 14b) is about five times larger than the maximum velocity of the corresponding primary intrusion in Section 3b. Unlike the primary mode in Figure 9, the equilibrium subharmonic mode has a
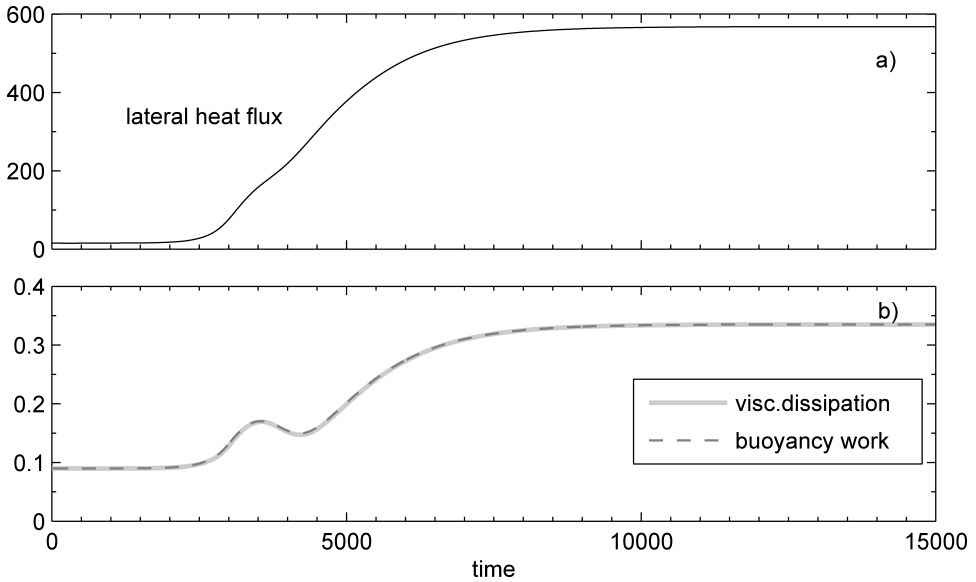
Figure 13. (a) The lateral heat flux as a function of time in the parameterized nonlinear calculation for the fastest growing secondary mode for $a = 0.05$. (b) The corresponding terms in the equation for the rate of change of the total kinetic energy; the Reynolds stress term (not shown) is essentially zero and the primary balance is between viscous dissipation and buoyancy work.
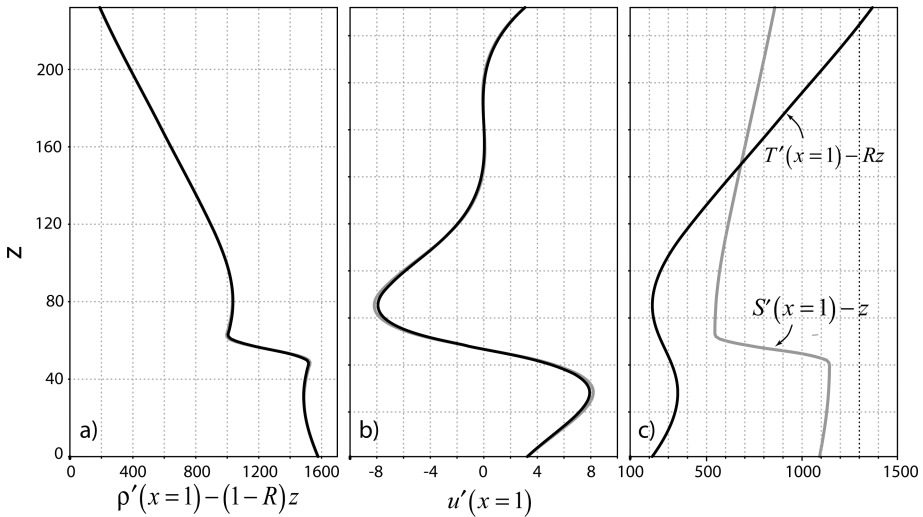

Figure 14. Profiles of total density (a) and lateral velocity (b) at $x = 0$ for $t = 7000$ (gray) and time-averaged for $8000 < t < 16000$ (black) for the secondary mode nonlinear calculation in Figure 13. (c) Temperature (black) and salinity (gray) profiles in the final steady state consist of a stable (salinity) interface surrounded by a salt finger favorable salinity inversions. The large salinity gradients and small temperature gradients are qualitatively similar to the observations (Fig. 1).
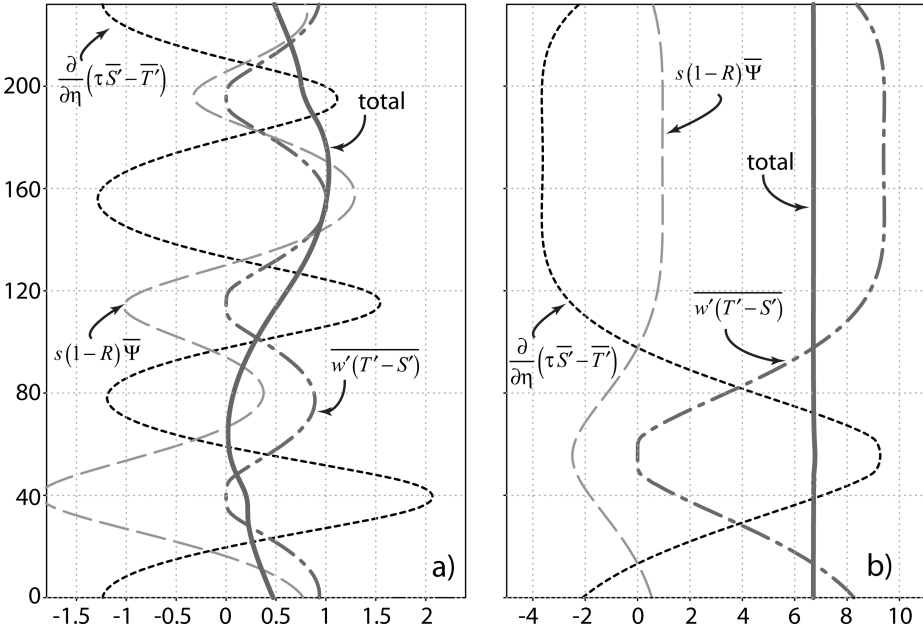
Figure 15. Profiles of the vertical buoyancy fluxes (4) due to molecular diffusion (short dashes), advection of the basic state (long dashes), salt finger convection (dash-dot) and their sum (thick line) at $t = 2000$ (a) and $t = 9000$ (b) for the secondary mode nonlinear calculation in Figure 13.

stronger salinity inversion in the salt-finger layer and a weak temperature inversion centered on the salinity interface (Fig. 14c).

To further elucidate the nonlinear evolution of the primary mode and the equilibration of the secondary mode we consider the buoyancy flux terms in the equation for the laterally averaged density perturbation (4). Vertical profiles of these terms are shown for an earlier time $t = 2000$ (Fig. 15a) when the solution is still dominated by the primary mode and a later time $t = 9000$ (Fig. 15b) when the secondary mode has equilibrated. Figure 15a shows that at $t = 2000$ the total buoyancy flux varies on the scale of the secondary mode although the individual flux components vary on the vertical scale of the primary intrusion. The amplification of the secondary mode (and the decay of the primary one) result from this particular distribution of the total buoyancy flux. As the primary mode decays, the vertical variation of the individual flux components changes accordingly (Fig. 15b) to reflect the length scale of the secondary intrusion. In the final steady state, the buoyancy production equilibrates again due to an approximate balance of the opposing molecular and salt finger fluxes (Fig. 15b). Compared to the initial salt finger flux (Fig. 15a) the flux in the final steady state is eight times stronger because the density ratio in the salt finger layer $R = 3.9$ is much smaller.

Table 3. The maximum nondimensional lateral velocity $U_{\max}$ and the horizontal heat flux $\langle \overline{u'T'} \rangle$ of the fastest growing subharmonic mode for different $a \equiv \bar{S}_x/\bar{S}_z$. Also given is the corresponding vertical domain size L_z. In all three calculations the Richardson number (7b) is $Ri_0 = 167.7$ and the density ratio in the salt finger layer is about 3.9.

$a \equiv \bar{S}_x/\bar{S}_z$	L_z	$U_{\max}$	$\langle \overline{u'T'} \rangle$
0.05	232.2	8.2	567.7
0.02	366.9	13.0	1419.2
0.01	519	18.3	2838.4

We made two similar calculations for $a = 0.02$ and $a = 0.01$, and the equilibrium intrusion heat flux and the maximum lateral velocity for these are given in Table 3. Figure 6 (Σ) shows that the subharmonic mode considered here also has $U_{\max}$ that increases linearly with the vertical wavelength:

$$U_{\max} = 0.035 h_{14 \times 3}; \tag{12a}$$

but the coefficient is about 50% larger than that for the primary intrusion (5). This differs from Simeonov and Stern (2008) where the velocity dependence on the vertical wavelength was approximately the same for the primary and the subharmonic modes. The discrepancy is probably due to the assumption in Simeonov and Stern (2008) that the slope of the subharmonic modes is equal to that of the primary intrusion. Table 3 also suggest the following inverse dependence of the heat flux of the subharmonic mode on a

$$\langle \overline{u'T'} \rangle = 28/a; \tag{12b}$$

this can be explained with simple dimensional arguments (Merryfield, 2000). An interesting fact obtained with these parameterized calculations is that the density ratio in the salt finger layer $R = 3.9$ and the Richardson number (7b) $Ri_0 = 167.7$ does not change with a. The density ratio and the Richardson number, however, are several times smaller than $R = 20$ and $Ri_0 = 791$ in the corresponding primary intrusion.

It is very plausible that the secondary equilibrium modes (plane waves) obtained here are themselves subject to subharmonic instability yielding even larger vertical and horizontal scales. Using the finite amplitude calculations for all wavelengths then one can obtain the dependence of the heat flux on the vertical scale with empirical coefficients that depend on a (cf. Simeonov and Stern, 2008). Preliminary simulations for longer vertical wavelengths suggest much stronger overturning instabilities and the associated mixing must be included in the parameterization of the small-scale fluxes (see for example Mueller *et al.*, 2007). These parameterizations must take into consideration the interaction of gravitational, salt finger and shear instabilities and would require further extensive DNS modeling. The development
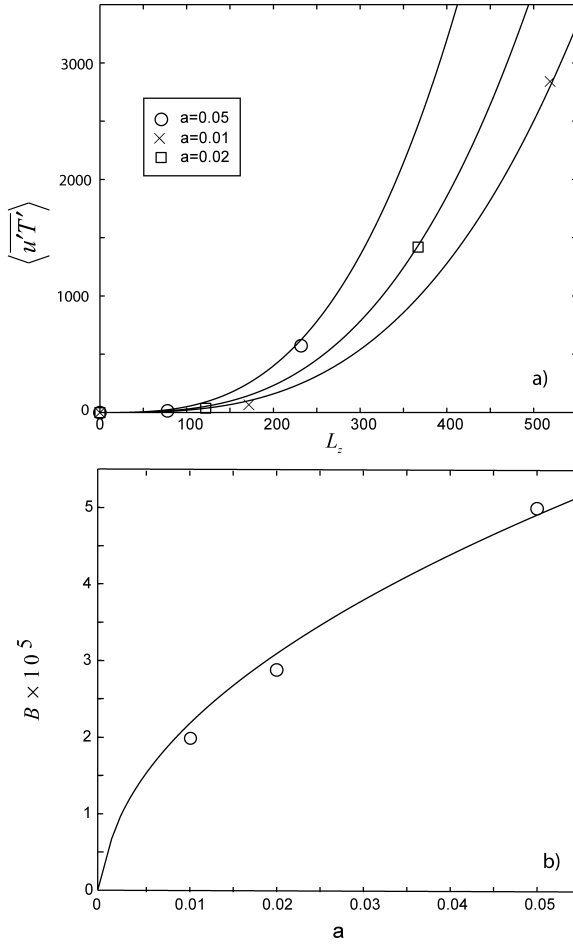
Figure 16. The lateral flux (a) as a function of the vertical wavelength L_z for different a; the solid lines are the cubic fits (13a). (b) The heat flux coefficient B as a function of a; the solid line is given by Eq. (13b).

of parameterizations appropriate for scales larger than the secondary modes considered here is beyond the scope of the present paper. In this paper, we use only the results for the fastest growing (Section 3b) and the secondary (this section) modes to determine a tentative dependence of the heat flux on the vertical scale. This is shown in Figure 16a, where the heat flux for different a is fitted by an ad-hoc cubic function of the vertical wavelength L_z:

$$\langle \overline{u'T'} \rangle = B(a)L_z^3. \tag{13a}$$

The coefficient $B(a)$ shown in Figure 16b appears to vary as the square root of a:

$$B(a) = 2.2 \times 10^{-4} a^{\frac{1}{2}}. \tag{13b}$$

6. Discussion

We have considered here finite-amplitude intrusions in double-diffusively stable verti-cal gradients such as those characterizing the front between the Indonesian Throughflow and Indian Ocean thermocline waters (Fig. 1). The finite amplitude evolution of the fastest growing intrusion of linear theory (Holyer, 1983) was studied with three-dimensional DNS which do not resolve explicitly the horizontal intrusion wavelength. The DNS showed that the molecularly-driven intrusions amplify until the modification of the vertical gradients results in the formation of salinity inversions that can support salt finger fluxes; the pre-dicted fingers were not strong enough to drive mixed-layer convection. It was found that the intrusion momentum remains in approximate buoyancy-viscous balance where the Reynolds stress work is negligible. This is consistent with Simeonov and Stern (2007) which show that a strong mixed layer convection is necessary for any significant Reynold stress effects. Because we study inifinitely wide fronts here, we do not expect Reynolds stress effects observed in finite width laboratory fronts (Krishnamurti, 2006). The present DNS also showed that the intrusions equilibrate because the salt fingers oppose the buoyancy anoma-lies produced by molecular diffusion. In addition to estimating the equilibrium intrusions amplitude we also used the DNS to obtain a new parameterization of salt finger fluxes for a limited range of shear and variable vertical gradients. In agreement with previous studies of the effect of shear on salt fingers (Fernandes and Krishnamurti, 2010; Kimura *et al.*, 2011) the new parameterization (8) predicts fluxes smaller than those in the absence of shear. The parameterization was tested in a two-dimensional calculation in which the horizontal intrusion wavelength is resolved explicitly; the predictions for $a = (0.05, 0.02, 0.01)$ were in good agreement with the corresponding DNS of Table 1.

Parameterized calculations were next used to investigate the subharmonic instability of the equilibrium primary intrusion. "Linearized" calculations for three different values of a (Section 4) showed that the fastest growing subharmonic mode has horizontal and vertical wavelengths which are respectively fourteen times and three times larger than those of the corresponding primary intrusion. The temperature and velocity spatial distribution of this mode consist of closed cells contained in a "carrier" plane-wave with a slope that is 3/14 of the slope of the primary mode. Parameterized calculations for the finite amplitude evolution of the fastest growing subharmonic mode (Section 5) showed that at large amplitude the latter is less influenced by the primary mode and becomes a pure plane wave. The subsequent equilibration of this larger-scale plane wave is similar to that of the primary mode and results mainly from salt finger buoyancy flux opposing the molecular one and buoyancy-viscous momentum balance.

The finite amplitude parameterized calculations were used to determine the dependence of maximum lateral velocity and the heat flux on the vertical wavelength. Denoting dimensional quantities with an asterisk, Eqs. (12a) and (13a,b) become:

$$U^*_{\max} = 0.014 N h^*_{14 \times 3}, \tag{14a}$$

$$F^* = 2.2 \times 10^{-4} \rho C_p a^{\frac{1}{2}} \left(\frac{L^*_z}{d} \right)^3 \frac{K_T \beta |\bar{S}_z|}{\alpha}, \tag{14b}$$

where $N = N_s \sqrt{1 - R}$ is the buoyancy frequency due to the total density gradient. Note that the thickness in (14b) is arbitrary while that in (14a) corresponds to the fastest growing secondary mode. Assuming $\alpha \bar{T}_x = \beta \bar{S}_x$ (14b) suggests the following horizontal eddy diffusivity:

$$K_H \equiv \frac{\alpha F^*}{\rho C_p \beta |\bar{S}_x|} = \frac{2.2 \times 10^{-4}}{a^{\frac{1}{2}}} \left(\frac{L^*_z}{d} \right)^3 K_T. \tag{15}$$

The coefficient in (14a) is about three times larger than that obtained in the laboratory experiments of Bormans (1992) for $R = -1$ and Ruddick *et al.* (1999) for $R = 0.6$. Compared to our previous DNS for finger favorable and diffusive stratification (Simeonov and Stern, 2007, 2008), the coefficient in (14a) is an order of magnitude smaller and suggests much weaker velocities. The small numerical coefficient in (14a) is a consequence of the very weak forcing (molecular diffusion) that drives the intrusions considered in this paper. Ruddick *et al.* (1999) rationalized the linear law (14a) by invoking a dimensional argument where the velocity scale is given by Nh and the constant multiplication factor is essentially a Froude number. While the latter implies a buoyancy-inertia balance, such a balance was not explicitly used in that paper as the intrusions were considered to be in a state of "continuous hydrostatic adjustment". To test the relevance of a buoyancy-inertia balance in the present experiments, we note that the buoyancy term $s\bar{\rho}'$ driving the lateral velocity (1a) contains the slope s which is also related to the thickness h, $s \sim h^{-2}$, from Eqs. (2) or (11b). Then, the density scale $\bar{\rho}' \sim h$ (reflecting the presence of salinity inversions) implies a buoyancy term $s\bar{\rho}' \sim h^{-1}$ such that a buoyancy-inertia balance $\bar{u}'^2 / h \sim s\bar{\rho}'$ results in a non-constant Froude number $\bar{u}' / h \sim h^{-1}$. On the other hand, $s\bar{\rho}' \sim h^{-1}$ and the buoyancy-viscous balance $\bar{u}' / h^2 \sim s\bar{\rho}'$ found in the present paper give the desired constant Froude number dependence $\bar{u}' / h \sim 1$.

It is interesting to discuss our numerical results in relation to the Indian Ocean observations in Figure 1. We estimate the following horizontal and vertical salinity gradients from Figure 1 - $\bar{S}_x = 0.6 \, \text{PSU}/550 \, \text{km} = 10^{-6} \, \text{PSU/m}$ and $\bar{S}_z = 0.2 \, \text{PSU}/200 \, \text{m} = 10^{-3} \, \text{PSU/m}$ which yield $a = 10^{-3}$ for the gradient ratio. Assuming also $\beta = 10^{-3} \, \text{PSU}^{-1}$ we obtain $d = 0.7 \, \text{cm}$. For these parameters the thickness of the fastest growing subharmonic mode is $h^*_{14 \times 3} = 11.5 \, \text{m}$ and the corresponding maximum velocity (14a) is $U^*_{\max} = 1.2 \, \text{mm/s}$. Figure 14c also suggests that the salinity interface has a thickness of about 1 meter. For comparison, the dominant interleaving scales in Figure 1b (about 30 m) are also characterized

with thin interfaces having a thickness of a few meters (see for example the 14°S profile at 75 m depth). Assuming an advection-diffusion balance, the molecular heat flux divergence across observed interfaces could be used in principle to make an order of magnitude estimate of the intrusion lateral velocity. Unfortunately, the publicly available 2 dbar data in Figure 1 is too coarse to estimate the molecular fluxes due to several rounds of filtering and averaging. Assuming intrusion thickness $L_z = 30$ m (Fig. 1b) and the same parameters as above, we also estimate from (15) a horizontal eddy diffusivity of $K_H = 82 \, \mathrm{m^2/s}$.

Like Simeonov and Stern (2008), the present model does not predict a preferred vertical wavelength. We believe that this results from the assumption of laterally unbounded gradients. The latter corresponds to infinite available potential energy that can be released through successively larger scale instabilities. In a finite width front, the maximum horizontal wavelength of a perturbation will be limited by the width of the front. This horizontal wavelength will be related uniquely to a vertical wavelength of the subharmonic modes. In this connection, it will be interesting to apply the parameterized model developed here to study the effect of variable mean gradients on the intrusions. The parameterized model can also be used to investigate the important effects of planetary rotation and baroclinicity (May and Kelley, 1997; Smyth, 2008) which are neglected here. Our parameterization is limited to relatively small intrusion scales where the effect of shear (cf. Radko and Stern, 2011; Kimura *et al.*, 2011) and overturning instabilities is negligible. Additional Direct Numerical Simulations will be needed to extend parameterizations to larger scales where the shear and gravitational instabilities are not negligible.

REFERENCES

Bormans, M. 1992. Effect of R_ρ on double diffusive interleaving. Deep-Sea Res., *39*, 871–884.

Fernandes, A. M. and R. Krishnamurti. 2010. Salt finger fluxes in a laminar shear flow. J. Fluid Mech., *658*, 148–165.

Gordon, A. L. 2005. Oceanography of the Indonesian Seas and their throughflow. Oceanography, *18*, 14–27.

Gordon, A. L., S. Ma, D. Olson, P. Hacker, A. Field, L. Talley, D. Wilson and M. Baringer. 1997. Advection and diffusion of Indonesian Throughflow water within the Indian Ocean South Equatorial Current. Geophys. Res. Lett., *24*, 2573–2576.

Holyer, J. Y. 1983. Double-diffusive interleaving due to horizontal gradients. J. Fluid Mech., *137*, 347–362.

Kerr, O. S. 1992. Two-dimensional instabilities of steady double-diffusive interleaving. J. Fluid Mech., *242*, 99–116.

Kimura, S. and W. D. Smyth. 2007. Direct numerical simulations of salt sheets and turbulence in a double-diffusive shear layer. Geophys. Res. Lett., *34*, L21610 10.1029/2007GL031935.

Kimura, S., W. D. Smyth and E. Kunze. 2011. Turbulence in a sheared, salt-fingering-favorable environment: Anisotropy and effective diffusivities, J. Phys. Oceanogr., *41*, 1144–1159.

Krishnamurti, R. 2006. Double-diffusive interleaving on horizontal gradients. J. Fluid Mech., *558*, 113–131.

Lele, S. K. 1992. Compact finite difference schemes with spectral-like resolution. J. Comp. Phys., *103*, 16–42.

Linden, P. F. 1974. Salt fingers in a steady shear flow. Geophys. Fluid Dyn., *6*, 1–27.

May, B. and D. Kelley. 1997. Effect of baroclinicity on double-diffusive interleaving. J. Phys. Oceanogr., *27*, 1997–2008.

Merryfield, W. J. 2000. Origin of thermohaline staircases. J. Phys. Oceanogr., *30*, 1046–1068.

Mueller, R. D., W. D. Smyth, and B. Ruddick. 2007. Shear and convective turbulence in a model of thermohaline intrusions. J. Phys. Oceanogr., *37*, 2534–2549.

Niino, H. 1986. A linear stability theory of double diffusive horizontal intrusions in a temperature-salinity front. J. Fluid Mech., *171*, 71–100.

Radko, T. and M. E. Stern. 2011. Finescale instabilities of the double-diffusive shear flow. J. Phys. Oceanogr., *41*, 571–585.

Ruddick, B. R., O. M. Phillips, and J. S. Turner. 1999. A laboratory and quantitative model of finite-amplitude intrusions. Dyn. Atmos. Oceans, *30*, 71–99.

Simeonov, J. and M. E. Stern. 2007. Equilibration of two-dimensional double diffusive intrusions. J. Phys. Oceanogr., *37*, 625–643.

—— 2008. Double-diffusive intrusions in a stable salinity gradient "heated from below." J. Phys. Oceanogr., *38*, 2271–2282.

Smyth, W. D. 2008. Instabilities of a baroclinic, double-diffusive frontal zone. J. Phys. Oceanogr., *38*, 840–861.

Stern, M. E. 1960. The "salt fountain" and thermohaline convection. Tellus, *12*, 172–175.

—— 1967. Lateral mixing of water masses. Deep-Sea Res., *14*, 747–753.

Stern, M. E., T. Radko, and J. Simeonov. 2001. Salt fingers in an unbounded thermocline. J. Mar. Res., *59*, 355–390.

Stern, M. E. and J. Simeonov. 2002. Internal wave overturns produced by salt fingers. J. Phys. Oceanogr., *32*, 3638–3656.

—— 2005a. The secondary instability of salt fingers. J. Fluid Mech., *533*, 361–380.

—— 2005b. Interaction of salt finger fluxes with shear flow. (Unpublished manuscript).

Talley, L. and M. Baringer. 1997. Preliminary results from WOCE hydrographic sections at 80°E and 32°S in the Central Indian Ocean. Geophys. Res. Lett., *24*, 2789–2792.

Walsh, D. and E. Carmack. 2003. The nested structure of Arctic thermohaline intrusions. Ocean Model., *5*, 267–289.